Forsch Ingenieurwes (2019) 83:635–644
https://doi.org/10.1007/s10010-019-00325-w

ORIGINALARBEITEN/ORIGINALS

Conventional high-strength nodular graphite iron as a substitute for austempered ductile iron (ADI)

Jochen Lohmiller[1] · Jürgen Hoffmeister[1] · Jörg Hermes[2]

Received: 15 March 2019 / Accepted: 27 May 2019

Abstract

Cast iron materials are becoming more widely used for large and complex components in mechanical engineering and drive technology. As a consequence of steadily increasing requirements, high-strength nodular graphite irons are in great demand. In order to fully exploit the potential of these materials, an in-depth characterization of their mechanical properties is necessary. This allows for reduced safety margins.

In this study, fatigue tests and accompanying microstructural characterization were performed comparatively on conventional nodular graphite iron EN-GJS-700-2. The material was characterized by very fine nodular graphite. The material has been cast into patterns of differently sized planetary carriers. Fatigue specimens were prepared from the cast components and tested in order to determine the fatigue limit. Microstructural characterization and fractography including optical and scanning electron microscopy were carried out.

As a key result, the correlation between mechanical and microstructural properties reveals the importance of fine and nodular graphite accompanied by the absence of microporosities or other casting defects in order to achieve high fatigue strengths. Moreover, a minor influence of the (pearlitic or ausferritic) matrix structure, in which the graphite is embedded, was determined. Consequently, the fatigue strength of conventional high-strength nodular cast iron may be rendered adequate by improving the graphite quality and eliminating casting defects. By understanding the correlations between mechanical properties and its microstructure, a precise load-carrying capacity can be obtained. Thus, the accurate design process of a cast component may avoid additional alloying elements and the expansive heat treatment in a salt bath that is necessary for ADI. The implementation of these findings can enhance the efficiency of cast components while reducing the costs.

✉ Jochen Lohmiller
jochen.lohmiller@sew-eurodrive.de

Jürgen Hoffmeister
juergen.hoffmeister@sew-eurodrive.de

Jörg Hermes
joerg.hermes@sew-eurodrive.de

[1] Development Gear Units, SEW-EURODRIVE GmbH & Co. KG, Ernst-Blickle-Str. 42, 76646 Bruchsal, Germany

[2] Innovation Mechanics, SEW-EURODRIVE GmbH & Co. KG, Ernst-Blickle-Str. 42, 76646 Bruchsal, Germany

Konventionelles hochfestes Gusseisen mit Kugelgrafit als Ersatz für Ausferrititsches Gusseisen mit Kugelgrafit (ADI)

Zusammenfassung

Gusseisenwerkstoffe werden immer häufiger für große und komplexe Bauteile im Maschinenbau und in der Antriebstechnik verwendet. Durch immer weiter steigende Anforderungen sind hochfeste Gusseisenwerkstoffe mit Kugelgrafit sehr gefragt. Um das Potential dieser Werkstoffe voll auszuschöpfen, ist eine gründliche Charakterisierung der mechanischen Eigenschaften nötig. Daraus können reduzierte Sicherheitsbeiwerte hervorgehen. In dieser Studie wurden Ermüdungsversuche und die zugehörige mikrostrukturelle Charakterisierung von konventionellem Gusseisen mit Kugelgrafit EN-GJS-700-2 durchgeführt. Der Werkstoff zeichnete sich durch extrem feinkugeligen Grafit aus. Der Werkstoff wurde in unterschiedlich große Modelle für Planetenträger gegossen. Die Ermüdungsproben wurden aus den gegossenen Bauteilen gefertigt und getestet mit dem Ziel die Dauerfestigkeit zu bestimmen. Mikrostrukturelle Charakterisierung und Fraktographie, einschließlich optischer und Rasterelektronenmikroskopie, wurden durchgeführt. Als eines der Hauptergebnisse zeigte die Korrelation von mechanischen und mikrostrukturellen Eigenschaften, dass feiner und nodularer Grafit, einhergehend mit der Abwesenheit von Mikroporositäten oder anderer Gussfehler, nötig ist, um hohe Dauerfestigkeiten zu erreichen. Zusätzlich wurde ein geringer Einfluss der (perlitischen oder ausferritischen) Matrixstruktur, in welche der Grafit eingebettet ist, festgestellt. Folglich kann die Dauerfestigkeit von konventionellem hochfesten Gusseisen mit Kugelgrafit, durch verbesserte Grafitstruktur und das Beseitigen von Gussfehlern, ausreichend groß sein. Durch das Verständnis der Wechselwirkung zwischen mechanischen und mikrostrukturellen Eigenschaften kann die genaue Beanspruchbarkeit des Werkstoffs bestimmt werden. Somit kann durch eine sorgfältige Auslegung eines gegossenen Bauteils ADI überflüssig werden und somit zusätzliche Legierungselemente und die teure Wärmebehandlung im Salzbad. Die Umsetzung dieser Erkenntnisse kann die Leistungsfähigkeit von gegossenen Bauteilen verbessern und gleichzeitig die Kosten reduzieren.

1 Introduction

Nodular cast irons cover a wide range of mechanical properties. Conventional (i.e. non-heat-treated) nodular cast irons (GJS) are represented by the standard DIN EN 1563:2011 [1] providing ultimate tensile strengths (*UTS*) from 350 to 900 MPa and fracture strains (ε_f) from 22 to 2%. Austempering, a two-stage heat treatment process consisting of austenitizing and subsequent isothermal tempering in a salt bath improves both, *UTS* and ε_f. These cast irons are named Austempered Ductile Irons (ADI). In the standard DIN EN 1564:2011 [2], their *UTS* ranges from 800 to 1400 MPa with ε_f from 10 to 1%. However, the improvement of mechanical properties leading to ADI is not cheap. Expensive alloying elements, e.g. nickel, are necessary in order to avoid a pearlitic transformation during cooling down to the isothermal austemper level. Even more expensive is the treatment in a salt bath, since the very large volume of the medium must be kept at a temperature typically between 250 and 400 °C.

In the standards, the mechanical properties of castings are defined up to a maximum relevant wall thickness of 200 mm for conventional nodular cast irons and 100 mm for ADI. The given mechanical properties—also found in the nomenclature of a specific material grade—originate from separately cast samples or cast-on samples. Mechanical properties of samples originating from real cast components are only informative. In practice, the mechanical properties obtained from separately cast or cast-on samples may not represent the mechanical properties from castings since cooling conditions differ. The difference increases with thicker castings. Beyond the validity of the standards, the properties are not defined for large components used in industrial applications but must be agreed between the customer and the foundry. So far, only quasi-static mechanical properties were mentioned, whereas information about cyclic properties for cast irons is rare. In the standards, fatigue properties are only stated informatively in the appendices and again originate from separately cast samples as well. However, compared to quasi-static properties, cyclic properties rely even more strongly on the specific microstructure of the cast component (e.g. graphite quality). For ADI, fatigue strength may even behave inversely with respect to *UTS* [3]. This underlines the importance of characterizing the cyclic properties of a specific cast component, since in many fields of application such as drive technology, the automotive industry, or the energy industry fatigue properties are the cornerstone of dimensioning.

In this study, fatigue tests and accompanying microstructural characterization were performed on conventional nodular graphite iron and compared to results from ADI which was processed and tested in the same way [4]. Nominally, the material grades were EN-GJS-700-2 and EN-GJS-900-8 respectively, determined by cast-on samples. However, the material under investigation originated from differently sized planetary carriers used in industrial planetary gear units. The same cast patterns were used for both materials. In the process, properties from real thick-walled

components were determined. These values can be used directly for the dimensioning of this type of components.

2 Experimental

All planetary carriers were cast by the iron foundry Hans Dhonau e.K. (Triberg, Germany) under real industrial conditions. Dhonau, a pure hand molding foundry, is an expert for thick-walled nodular graphite castings. Dhonau's casting technique is characterized by the extensive use of cooling chills and no use of risers. The raw material generally consists of more than 50% Brazilian pig iron and only about 20% steel scrap. The chemical composition was held in a narrow range as follows: C ≈ 3.56%, Si ≈ 2.14%, Mn ≈ 0.06% and Mg ≈ 0.04%. Moreover, Cu was alloyed (≈1.50%) because of its pearlitizing effect to account for the heavy wall thickness. Sn was additionally alloyed (0.06%) for two variants. For details about the casting process, please refer to Ref. [4].

All results in this study were obtained from samples prepared out of planetary carriers and not from separately cast or cast-on samples. Most samples were prepared from the bearing seat ("B") since it is the thickest solid part of each carrier and also contains the most critical spot at the undercut towards the cage of the carrier. Also samples were prepared from the solid output shaft ("S") since it is the most homogeneous region of the carrier. All samples, except the series P022-B-c, were prepared out of a depth of 20 mm below the final dimension of the bearing seat ($d_{F,B}$) and the solid shaft ($d_{F,S}$) respectively (see Fig. 1). The effective diameter corresponds to the diameter of the raw part.

First, cylinders were cut out by wire-cut EDM. Shape B tensile samples with $d_0 = 10$ mm were produced according to DIN 50125:2009 [5]. Tension-compression fatigue samples were designed in consideration of ASTM E 466-07 [6] and similarly to Ref. [4]. The stress concentration factor was 1.04 and the probed volume was around 1571 mm³. After turning, the gauge section was polished with a 6 µm polish.

For each series, at least 3 tensile samples were tested on a Zwick Z100. The test was carried out according to DIN EN ISO 6892:2009 [7]. Similarly to the previous study [4], tension-compression fatigue tests with a stress ratio $R = -1$ were carried out on an electromagnetic Sincotec MAG 150 kN. The staircase method was applied and fatigue limits with a failure probability of 50% $S_{f,tc,Pf=50\%}$ and 2.5% $S_{f,tc,Pf=2.5\%}$ were determined from at least 12 valid tests. Tests were carried out up to an ultimate number of cycles 10^7. After the failure of the fatigue samples, the fracture surface was investigated with a stereomicroscope and to some extent by an ASPEX express scanning electron microscope (SEM). An Olympus BX51M light microscope was used for optical microscopy of unetched and etched microsections. The graphite structure was analyzed statistically by the cast iron module of the Olympus software Stream Motion.

3 Results

The results of the material investigations of differently sized GJS planetary carriers are presented below. Table 1 below provides an overview of the different components and materials under investigation. The designation of a test series consists of the size of the planetary carrier and the area under investigation. In test series P022-B-c, "c" stands for contour, as samples were not prepared 20 mm beneath the final contour as for all other series (e.g. P022-B: pitch diameter = 180 mm), but the probed sample volume was located directly beneath the final contour (pitch diameter = 210 mm, while $d_{F,B} = 220$ mm).

First, the microstructures of the materials were analyzed. In Fig. 2, the micrographs of all GJS test series are presented. From the unetched micrographs in the left-hand column, it can be seen that the size of graphite nodules increases with increasing component size or rather increasing effective diameter. This is confirmed by automated software

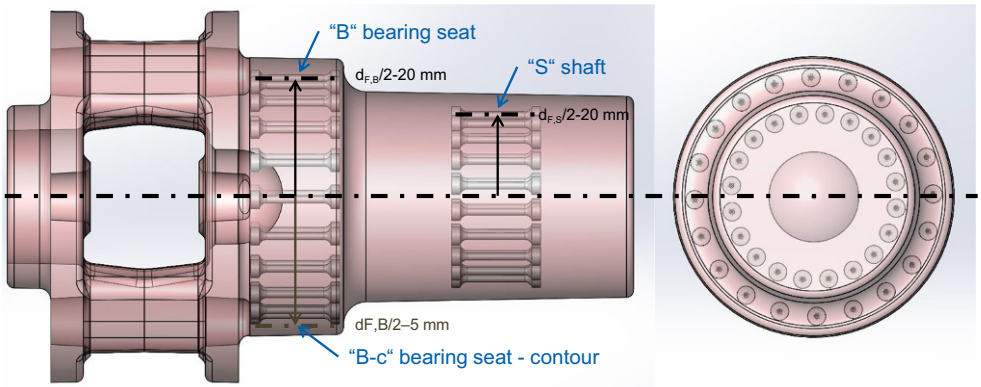

Fig. 1 CAD model of a raw planetary carrier P072. In general, the pitch diameter where samples are extracted is 20 mm below the final contour of all sizes ("B", "S"). For "B-c", the probed sample volume represents the first 10 mm below the final contour

analysis of the graphite. Doing so, the area A of each nodule was measured and then an equivalent nodule diameter was calculated according to $d_g = \sqrt{4A/\pi}$. The mean equivalent nodule diameter ranged from 14 µm for the smallest cross-section (P032-S) up to 19 µm for the largest cross-section (P102-B). Otherwise, nodule density decreased from 495 1/mm² to 220 1/mm². Nodularity was larger than 90% for all test series with the exception of P102-B (79%). According to EN ISO 945-1:2010 [8], the graphite content ranged from 7 to 9%.

The etched micrographs are displayed on the right-hand side of Fig. 2. All samples show a pearlitic microstructure, and in some samples small ferritic islands are visible. Furthermore, it is noticeable that the pearlite becomes coarser with increasing effective diameter.

In the following, the results of quasi-static tests are presented. Table 2 shows the minimum and mean values of the results of tensile tests. At least 3 samples were tested for each series.

Fig. 3 displays the mean values from tensile tests as a function of effective diameter. The strength values lie considerably above the line according to the FKM guideline calculated for GJS-700-2 (solid line). Mechanical data for GJS types are defined up to an effective diameter of 400 mm according to DIN EN 1563 [1] and the FKM guideline [9]. For larger diameters, the dashed line is added as a visual guide. The lowest strength values were found for P102-S. The trends will be discussed in Sect. 4.1. The fracture strains ε_f, shown in Fig. 3c are in the range between 2.8 and 5.5%, clearly above the value of 1% required for cast parts according to DIN EN 1563 [1] (see dotted line). The square stands for samples from the output shaft ("S") of a carrier (most homogeneous section), the upright triangle stands for samples from the bearing seat ("B") of a carrier (thickest solid section), the reversed triangle for sample position straight beneath the final contour ("c"), and the open symbols for carriers with a significant appearance of Mg oxides (see below).

The results from tension/compression fatigue tests are presented below (Table 3). The fatigue strength is given with a failure probability $P_f = 50\%$ ($S_{f,tc,Pf=50\%}$) and $P_f = 2.5\%$ ($S_{f,tc,Pf=2.5\%}$). The scatter band T was calculated according to $T = S_{f,tc,Pf=97.5\%}/S_{f,tc,Pf=2.5\%}$. Based on the FKM guideline, the ratio $f_{w,\sigma}$ was obtained from $f_{w,\sigma} = S_{f,tc,Pf=50\%}/UTS$.

The results from fatigue tests are displayed in Fig. 4 as a function of effective diameter. Similarly to UTS, the fatigue strength $S_{f,tc}$ decreases with increasing diameter (see Fig. 4a). The green data points correspond to a failure probability of $P_f = 50\%$, while orange corresponds to $P_f = 2.5\%$. The black solid line shows the trend according to the FKM guideline with $f_{w,\sigma} = 0.34$ and corresponds to a failure probability of $P_f = 2.5\%$. The 50% fatigue limits of all series tested are above the trend line from FKM. Regarding the data points with $P_f = 2.5\%$, the open symbols (Mg oxides) and the data point beyond the validity of the black trend line (P102-B) are below the trend according to the FKM guideline. The logarithmic fits are discussed in Sect. 4.1. Furthermore, in Fig. 4b the scatter band T increases with increasing effective diameter d_{eff} and is highest for the data points with open symbols Fig. 4c. displays the ratio $f_{w,\sigma}$ for each individual test series and it can be seen that the determined values are close to $f_{w,\sigma} = 0.34$ from the FKM guideline.

After fatigue testing, the fracture surfaces were examined. Two different failure mechanisms were found and are shown in Fig. 5 by exemplary SEM micrographs. In one case fatigue cracks originated at an accumulation of some coarser graphite nodules near the surface of a sample (Fig. 5a). The critical nodules measured approximately 50 to 75 µm in diameter, while the mean nodule diameter ranged from 14 to 19 µm depending on component size. Macroscopically, no defect was seen on the fracture surface. In the second case, a defect was seen clearly by the naked eye. SEM micrographs showed volume defects measuring approximately 500 µm to 1 mm in length (Fig. 5b,c). Defects were found close to the sample surface. Some defects were in contact with the free sample surface, some were entirely located beneath the sample surface at a maximum depth of 1 mm. EDX analyses revealed Mg oxides as the origin of fatigue crack growth (Fig. 5d).

Compared to high strength steels, where non-metallic inclusions (e.g. Al oxides, $d \approx 10$–100 µm) were the origin

Table 1 Overview of all types under investigation

Designation	Material	Size of carrier	Area under investigation	Effective diameter (mm)	Pitch diameter of sampling (mm)
P022-B	GJS Std	P022	Bearing seat	232	180
P022-B-c	GJS Std	P022	Bearing seat	232	210
P032-S	GJS Std	P032	Output shaft	177	125
P072-S	GJS Std	P072	Output shaft	280	220
P072-B[a]	GJS Sn[a]	P072	Bearing seat	384	320
P102-S	GJS Std	P102	Output shaft	372	300
P102-B[a]	GJS Sn[a]	P102	Bearing seat	492	420

[a]0.06% Sn was added

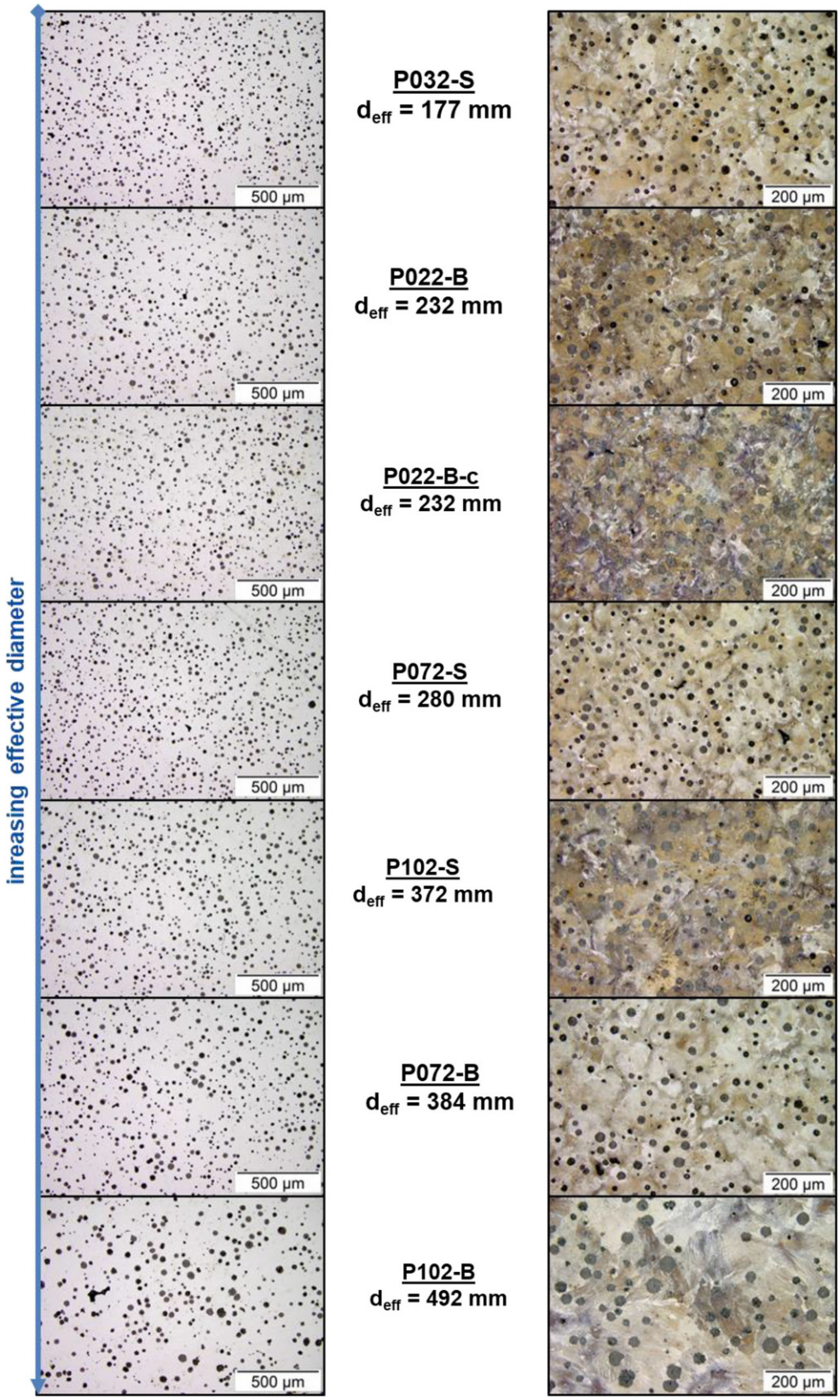

Fig. 2 Results from microstructural analysis. Unetched (left) and etched (right) micrographs from fatigue samples from differently sized planetary carriers. The probed volume is located close to the fracture surface of fatigue samples (i.e. 20 mm beneath the final contour of each carrier). Exception: P022-B-c, directly beneath the final contour

Table 2 Summarized results from tensile tests. The first values are the minimum, the second the mean values

Designation	Effective diameter d_{eff} (mm)	Ultimate tensile strength UTS (MPa)	Yield strength YS (MPa)	Fracture strain ε_f (%)
P022-B	232	814/825	494/496	3.9%/4.3%
P022-B-c	232	720/769	491/503	2.1%/2.8%
P032-S	177	801/821	486/494	3.7%/4.6%
P072-S	280	785/793	472/476	5.0%/5.5%
P072-B[a]	384	798/801	489/495	3.3%/3.5%
P102-S	372	663/672	398/400	4.2%/4.4%
P102-B[a]	492	721/779	414/478	2.5%/3.2%

[a]0.06% Sn was added

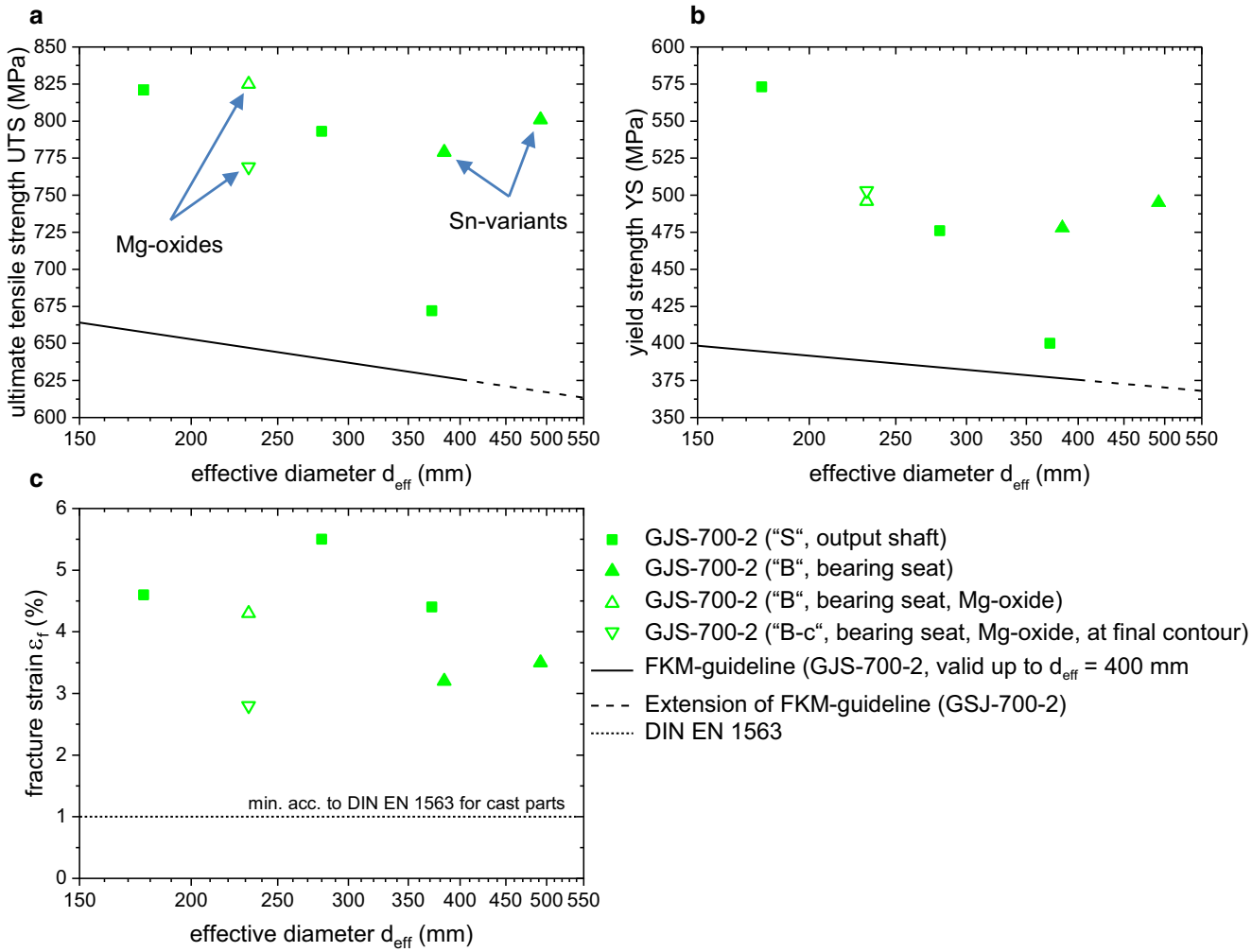

Fig. 3 Results from tensile tests. **a** *UTS*, **b** *YS*, and **c** ε_f as a function of effective diameter d_{eff}. The solid line shows the trend according to the FKM guideline

of fatigue failure, the Mg oxides were about one order of magnitude larger. However, the depth from surface where failure originated was comparable [10].

The relative occurrence of both failure mechanisms was evaluated statistically for all samples tested. The results are shown in Fig. 6. Samples from test series P022-B and P022-B-c predominantly failed due to clearly visible volume defects (Mg oxides), while for the other series no macroscopic defects could be found on the fracture surface and SEM analyses suggested failure due to coarser graphite nodules.

Table 3 Summarized results from tension/compression fatigue tests

	Effective diameter	Fatigue strength		Scatter band	
	d_{eff} (mm)	$S_{f,tc,Pf=50\%}$ (MPa)	$S_{f,tc,Pf=2.5\%}$ (MPa)	T	$S_{f,tc,Pf=50\%}$/UTS (MPa)
P022-B	232	263	215	1.45	0.32
P022-B-c	232	243	202	1.41	0.32
P032-S	177	300	275	1.18	0.37
P072-S	280	279	244	1.29	0.35
P072-B[a]	384	257	217	1.37	0.32
P102-S	372	249	218	1.28	0.37
P102-B[a]	492	226	194	1.35	0.29

[a]0.06% Sn was added

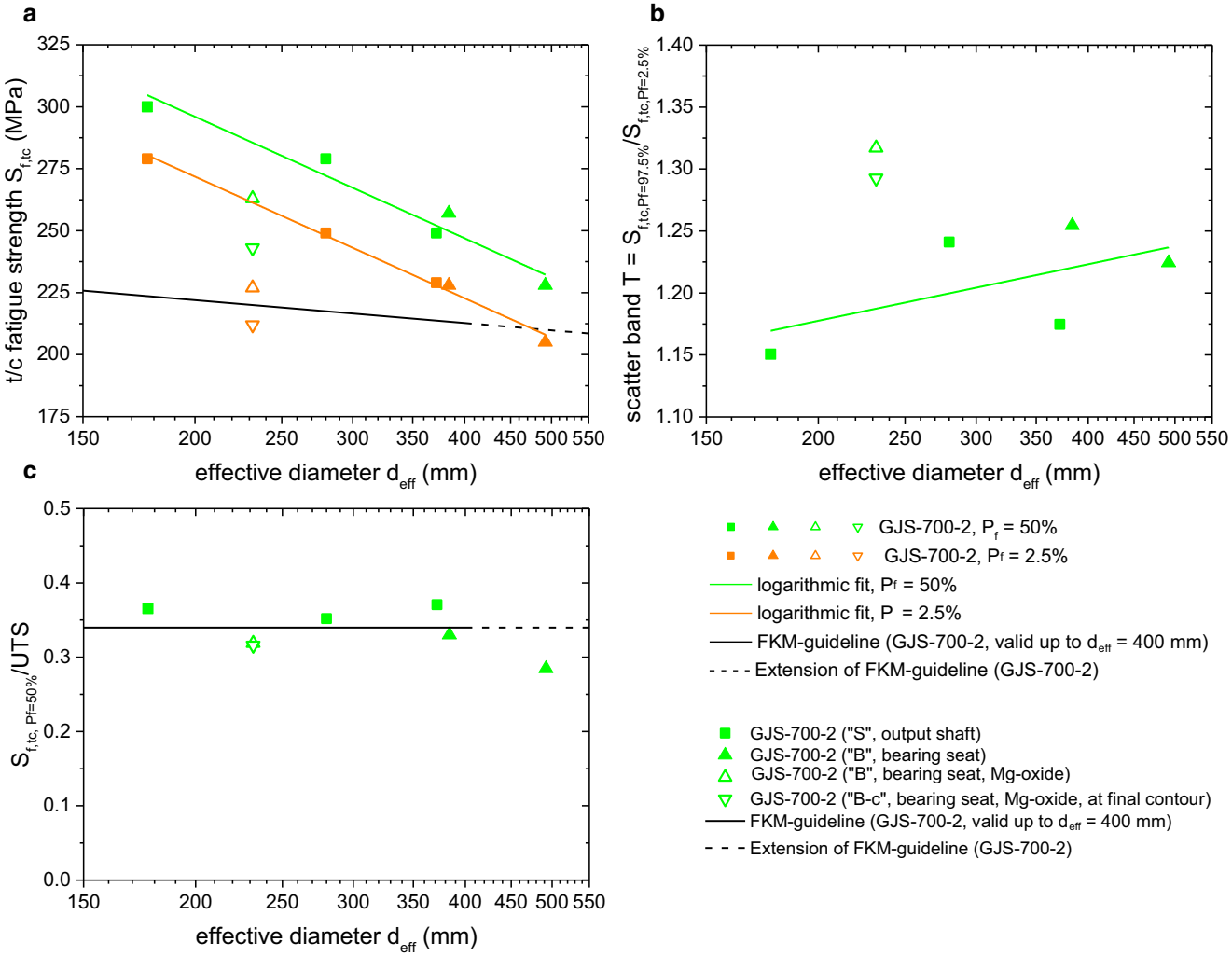

Fig. 4 Results from tension/compression fatigue tests. **a** $S_{f,tc}$, **b** scatter band T, and **c** $S_{f,tc}/UTS$ as a function of effective diameter d_{eff}

4 Discussion

The discussion is subdivided into two parts: First, the results of GJS are discussed with respect to the microstructure-property relationship, the technological size effect, and failure mechanisms. Afterwards, the GJS results are discussed with respect to the ADI results from the former study of the authors [4].

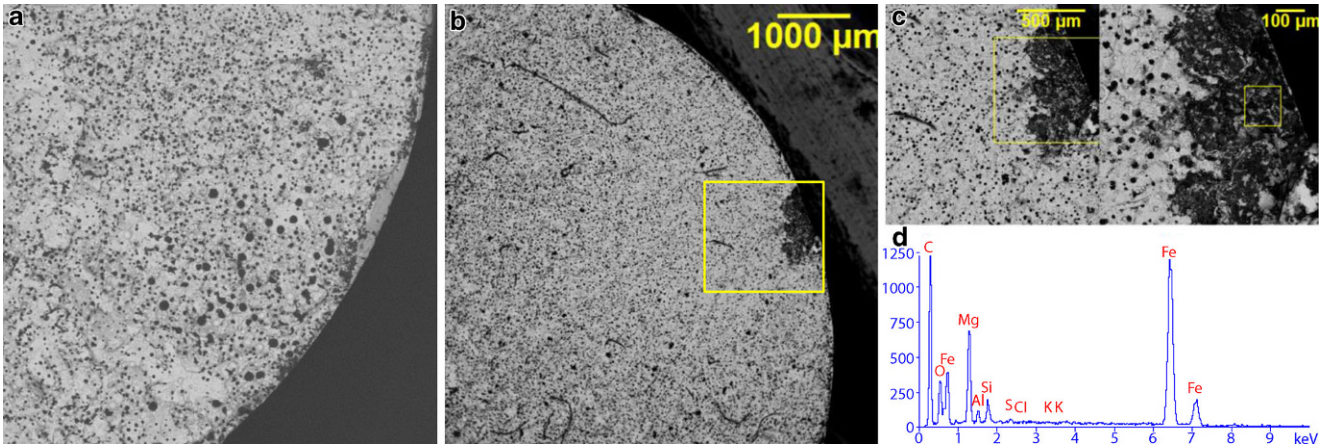

Fig. 5 Results from SEM and EDX analyses. **a** and **b** show two different failure mechanisms. **c** In the second case the crack originates at Mg oxides as **d** EDX reveals

4.1 GJS-700-2

For the discussion, it is essential to reiterate that the material was modified slightly during the study by alloying about 0.06% Sn to the standard composition to account for the largest effective diameters (P072-B and P102-B). Considering *YS* and *UTS* from tensile tests as a function of effective diameter, the data points of P102-S stand out (see Fig. 3, lowest strength). Only examining the data points from the standard chemical composition and ignoring the two data points from the Sn variants (two largest diameters, solid upright triangles), a pronounced size effect would exist, much more pronounced than the trend from the FKM guideline would suggest. However, alloying Sn to the standard composition can significantly help to increase quasi-static strength and reduce the technological size effect to a minimum with overall high values well above the black trend line.

The fracture strains, shown in Fig. 3c, may scale with the small amount of ferritic grains, which were arranged in between the pearlitic grains and especially around graphite nodules (cf. Fig. 2). The fact, that fracture strain of P022-B-c is distinctly smaller than of P022-B supports the hypothesis, since samples prepared at the final contour ("c") should have less ferrite than samples at the standard position (20 mm below the final contour) due to faster solidification and cooling. Moreover, for the Sn-variants P072-B and P102-B less fracture strain was found, which could be explained with the pearlitzing effect of Sn.

Regarding the fatigue strength Sn also helps to confine the technological size effect for cyclic properties to an unavoidable minimum. Sn with its pearlitizing effect yields a predominantly constant matrix structure over the different component sizes (cf. Fig. 2, right column). Hence, the technological size effect of fatigue strength can be correlated with the evolution of graphite structure. In the left column of Fig. 2, it can be seen that nodules increase with

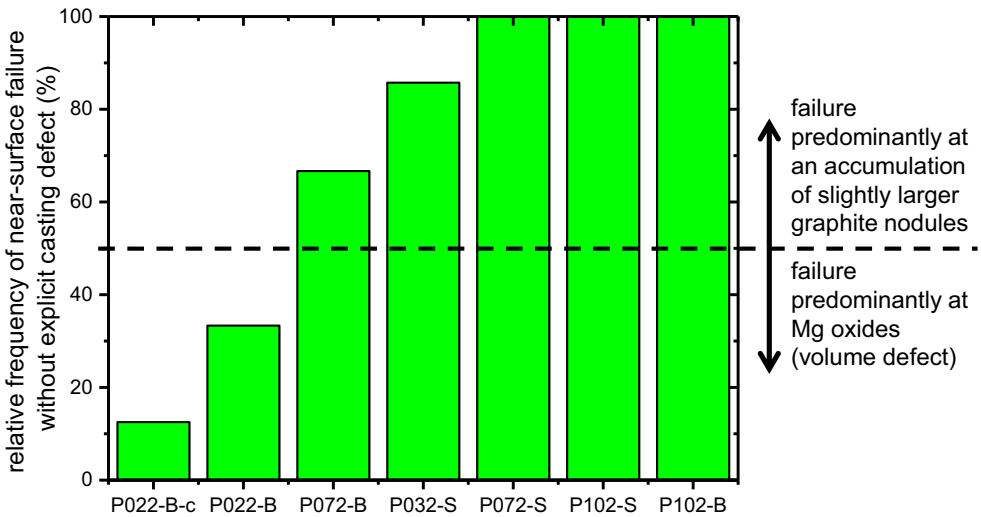

Fig. 6 Statistical evaluation of the two different failure mechanisms found

increasing d_{eff} and statistical evaluation revealed an increase from 14 to 19 µm from the smallest to the largest component cross-section. The trend of larger nodules for larger component sizes or rather increasing d_{eff} originates from the retarded cooling conditions for larger components.

Surprisingly, microporosities (or microshrinkage) were irrelevant with regard to the failure mechanism. In the unetched micrographs (Fig. 2, left), pores were small-sized and rare, and furthermore no pores were found as the origin for cracks during the SEM analyses (Fig. 5). This is even more astonishing when we remember that the material originated from real components with diameters up to 500 mm and not from cast-on or separately cast samples. In contrast, in the literature, pores were found to be the origin of fatigue failure for pearlitic [11] and ferritic-pearlitic [12] grades, although the raw material was of much smaller size [11].

However, carelessness—e.g. during slagging off—provokes the formation of Mg oxides as seen with P022-B and P022-B-c. At a certain frequency, these oxides become failure-relevant as seen in Figs. 5b and 6. Fatigue strength decreases significantly due to the altered failure mechanism (open symbols in Fig. 4a), and the scatter band increases (Fig. 4b). Conversely, the quasi-static strengths do not show an impact of Mg oxides since failure during tensile testing originated at the sample surface despite oxides in the volume of the sample. Unfortunately, activities regarding quality assurance are limited to tensile tests at the most. Consequently, an inferior material quality may remain undetected unless quality checks are conducted on machined surfaces of cast components.

Similarly to our former study [4], extreme value statistics based on the approach by Murakami [10] were applied to GJS to estimate the largest graphite nodule $d_{g,\ max}$ in the probed sample volume ($V = 1571\ mm^3$). As discussed above, the role of microporosities was insignificant, so statistical evaluation was carried out only for graphite. Assuming the largest defect (i.e. largest nodule) is relevant for failure, a microstructure-property relationship was established to estimate the fatigue strength based on the maximum nodule diameter: $S_{f,tc,Pf=50\%} \propto d_{g,\ max}^{-0.37}$, which is in full agreement with the literature [13]. Hence, assuming a constant matrix structure, decreasing fatigue strength can be correlated with an increasing maximum nodule diameter and can be described by a power-law fit. In compliance with the literature [12], a dependency on nodularity was not found since overall nodularity is very high and differences between the test series were only minimal (~94% ± 1%) with the exception of P102-B.

4.2 GJS-700-2 vs. ADI-900-8

Since fatigue properties are of major interest for the dimensioning of components for drive technology and the automotive industry, the discussion is focused on the tension/compression fatigue strength. In Sect. 4.1 and in Fig. 4, it was shown that—in addition to a fine nodular graphite structure—the absence of casting defects, such as Mg oxides, is necessary to obtain a high level of fatigue strength for GJS. If we neglect the data points in Fig. 4a where Mg oxides cause inferior fatigue strength (open symbols), the remaining data points of $S_{f,tc,Pf=50\%}$ can be fitted with a logarithmic fit function (green line). This line and, in addition, the fit functions of ADI from our former study [4] are displayed in Fig. 7: The red line shows the fit for the GJS-900-8 developed between SEW-EURODRIVE and Dhonau and the blue line for the commercial reference (also GJS-900-8). Additionally, the lines from the FKM guideline are displayed for GJS-700-2 and ADI-900-8. The transition from the solid to the dashed line indicates the range in which material properties are defined for GJS and ADI respectively, i.e. the dashed line is rather speculative. It can be seen that the GJS from this study can be classified between Dhonau-SEW ADI and the ADI reference, slightly closer to the superior material. The graph shows that (i) the high-quality GJS developed and investigated in this study has a considerably higher fatigue strength than an imperfect ADI and (ii) the high-quality GJS yields only about 10% less fatigue strength than the high-quality ADI. Compared to the trend lines according to the FKM guideline, GJS clearly exceeds the line for GJS-700-2 and even for GJS-900-8 in the valid diameter range up to 200 mm. Overall, it can be seen that the technological size effect for all 3 materials for such a large effective diameter exceeds the one suggested by the FKM guideline, although it was counteracted by modifying the alloy composition for GJS and the heat treatment for ADI.

Both GJS and Dhonau-SEW ADI are characterized by a very fine nodular graphite structure, in contrast to the ADI reference. Apparently, the microstructure obtained after casting (graphite structure, absence of casting defects) is of particular importance. The matrix structure plays a minor role. The large difference in the fatigue strength (~25%) between Dhonau-SEW ADI and the ADI reference is primarily linked to the considerable difference in graphite structure (and microporosities), since the matrix structure was found to be comparable by means of retained austenite. In the case of GJS and Dhonau-SEW ADI, the difference in fatigue strength is only about 10% when the graphite structure is comparable, and can be explained by the difference between the pearlitic and ausferritic matrix.

As a consequence, a high-quality GJS can be adequate for many applications where ADI was previously in use.

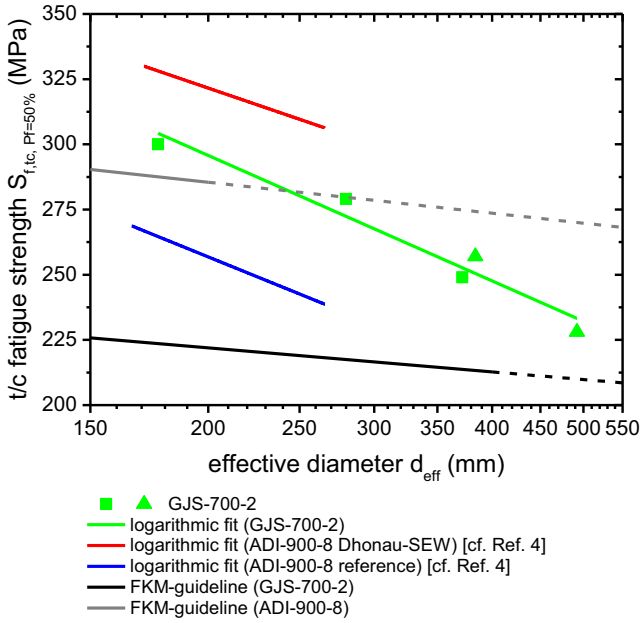

Fig. 7 Summarizing plot of fatigue strengths comparing GJS from this study with two types of ADI [4] and with trends from the FKM guideline

The following advantages of GJS result in an increase in efficiency and a reduction of costs for cast components: (i) no expansive alloying elements (e.g. nickel) are required, (ii) no expansive heat treatment in salt bath is required, and (iii) a reduced machining time is achieved, due to reduced overall hardness and no transformation of retained austenite to martensite during machining.

5 Summary and conclusions

In this study, a high-quality GJS-700-2 was investigated. Samples for tension-compression fatigue testing were prepared from thick-walled planetary carriers. Accompanying microstructural analyses and fractographical investigations were carried out. Finally, the results were compared to results from GJS-900-8 (ADI) processed in the same patterns with the same casting technique. The findings can be summarized as follows

- The high-quality GJS is characterized by a very fine nodular graphite structure and the absence of casting defects such as Mg oxides. Microporosities were so small and rare that they were not relevant to fatigue failure, but cracks originated predominantly at an accumulation of slightly larger graphite nodules close to the sample surface.
- While the technological size factor for quasi-static strength is comparable to the one suggested by the FKM guideline, the decrease with increasing effective diameter is more pronounced for fatigue strength. In the investigated diameter range from 150 to 500 mm, a scaling behavior between fatigue strength and maximum nodule diameter was found according to $S_{f,tc} \propto d_{g,\ max}{}^{-0.37}$, assuming a constant matrix structure.
- Compared to ADI, it was found that the difference in matrix structure only yields about 10% less fatigue strength for the pearlitic matrix compared to the ausferritic, provided that very fine nodular graphite exists in both cases. Far more important than the matrix is the graphite structure, as it accounts for a difference of 25%, provided that the matrix structure is comparable [4].
- The study showed that, in many cases, high-quality GJS may be used as a substitute for ADI for thick-walled cast components. As a result, this enhances the efficiency of cast components while reducing the costs.

Acknowledgements The authors gratefully acknowledge Hans Dhonau and Michel Ansorg (both Eisengießerei Hans Dhonau e.K.) for their great support providing the material and for fruitful discussions.

References

1. DIN EN 1563:2011, Founding—Spheroidal graphite cast irons
2. DIN EN 1564:2011, Founding—Ausferritic spheroidal graphite cast irons
3. Lin CK, Wei JY (1997) High cycle fatigue of austempered ductile irons in various-sized Y-block castings. Mater Trans Jim 38(8):682–691
4. Lohmiller J, Hoffmeister J, Hermes J, Ansorg M, Dhonau H (2017) Development and investigation of austempered ductile iron (ADI) for thick-walled gear components. Forsch Ingenieurwes 81:253–263
5. DIN 50125:2016, Testing of metallic materials—Tensile test pieces
6. ASTM E 466—07, Standard Practice for Conducting Force Controlled Constant Amplitude Axial Fatigue Tests of Metallic Materials
7. DIN EN ISO 6892-1:2009, Metallic materials—Tensile testing
8. DIN EN ISO 945-1, Microstructure of cast irons—Part 1: Graphite classification by visual analysis
9. Haenel B, Haibach E, Seeger T, Wirthgen G, Zenner H (2012) FKM Guideline—Analytical Strength Assessment of Components in Mech. Eng., VDMA, Frankfurt, 6th edn. in German, Germany
10. Murakami Y (2002) Metal Fatigue: Effects of Small Defects and Nonmetallic Inclusions. Elsevier, Oxford
11. Shiraki N, Watanabe T, Kanno T (2015) Relationship between Fatigue Limit and Defect Size in Spheroidal Graphite Cast Iron with Different Graphite Spheroidization Ratios and Microstructures. Mater Trans 56(12):2010–2016
12. Bergstroem J, Burman C, Svensson J, Jansson A, Ivansson C, Zhou J, Valizadeh S (2016) Very High Cycle Fatigue of Two Ductile Iron Grades. Steel Res Int 87(5):614–621
13. Tanaka Y, Yang Z, Miyamoto K (1995) Evaluation of Fatigue Limit of Spheroidal Graphite Cast Iron. Mater Trans 36(6):749–756